Journal of Power Sources 257 (2014) 205–212

Contents lists available at ScienceDirect

Journal of Power Sources

journal homepage: www.elsevier.com/locate/jpowsour

Lithium intercalation into single-walled carbon nanotubes network electrode: Storage mechanisms and impurity effects

Luciano Andrey Montoro [a], Elaine Yoshiko Matsubara [b], José Maurício Rosolen [b,*]

[a] Universidade Federal de Minas Gerais, Departamento de Química, 31270-901 Belo Horizonte, MG, Brazil
[b] Universidade de São Paulo, Departamento de Química-FFCLRP, 14040-901 Ribeirão Preto, SP, Brazil

HIGHLIGHTS

- Lithium chemical diffusion coefficient SWCNT network electrode can achieve 10^{-4} cm^2 s^{-1}.
- The experimental specific capacity of high-purity SWCNT network electrode is 400 mAh g^{-1}.
- Amorphous carbon damages the lithium intercalation in SWCNT.
- Lithium insertion can provoke an electronic transition of the semiconducting-metal type in the SWCNT network electrode.

ARTICLE INFO

Article history:
Received 21 November 2013
Received in revised form
31 January 2014
Accepted 2 February 2014
Available online 8 February 2014

Keywords:
SWCNT
Lithium
Carbon
Diffusion

ABSTRACT

This is a detailed study of how impurities can affect the mechanisms of lithium storage in composite electrodes consisting of a three-dimensional single-walled carbon nanotube (SWCNT) bundles network. To remove impurities such as fullerenes, amorphous carbon, catalyst, and nanographite, we submitted the SWCNT bundles to an appropriate chemical treatment before using them to prepare the electrode. Then, we analyzed how this treatment influenced electrode potential, fading capacity, and specific capacity. Additionally, we evaluated the electrode prepared with high-purity SWNCT bundles by galvanostatic intermittent titration, to obtain lithium transport parameters under thermodynamic conditions. We achieved an intrinsic specific capacity of 400 mAh g^{-1} for the purified SWCNT bundles prepared by an arc-reactor method. The transport parameters revealed that the electrode underwent electronic transition of the semiconducting-metal type. The chemical diffusion coefficient ranged from 10^{-4} to 10^{-18} cm^2 s^{-1} with decreasing electrode potential.

1. Introduction

Carbon nanotubes (CNTs) are attractive materials to develop many types of electrochemical devices. In addition to their classical application as electroactive material, CNTs can provide electrodes free of polymer binder. Such electrodes display enhanced mechanical properties and electronic conductivity, and they can support temperature peaks associated with the joule effect in storage devices [1–3]. CNTs include not only regular single-walled (SWCNT) and multi-walled carbon (MWCNT) nanotubes, but also disordered structures such as the fish-bone, coiled, and cup-stacked arrangements, which have different structural ordering and agglomeration. Concerning energy storage devices, CNT-based materials are particularly interesting: they bear many sites to intercalate and/or adsorb chemical species, transport electrons very fast, exhibit good chemical and thermal stability, and can originate from different carbon sources. The CNT surface can incorporate many chemical substances and nanomaterials that can also be electroactive, which making CNTs potentially applicable in both cathodic and anodic lithium ion batteries, supercapacitors, fuel cells, and other energy devices. However, in the field of carbon nanostructures, it is well known that the synthesis method and the processing methodologies used to prepare CNTs determine the final CNT properties, structural ordering, chirality, diameter distribution, tube length, defects, and intertube interactions (bundling), and also the impurities that will exist in the samples (e.g., amorphous carbon, residual catalysts, fullerenes, and nanographite particles). Because many factors can outline CNT-based electrode performance, establishing the electrochemical behavior of CNT materials is not an easy task.

In the specific case of lithium ion batteries, several studies on the electrochemical performance of CNT-based materials during

* Corresponding author.
E-mail address: rosolen@ffclrp.usp.br (J.M. Rosolen).

0378-7753/$ – see front matter © 2014 Elsevier B.V. All rights reserved.
http://dx.doi.org/10.1016/j.jpowsour.2014.02.002

energy storage revealed that they behave distinctly, generating different energy capacities, reversibility, and lifetime even when the materials originate from similar procedures [4–10]. Countless misconceptions have derived from the results reported to date, because authors usually employ different purification methodologies to remove the byproducts and residual catalysts, not to mention that they attempt to induce physicochemical modifications such as structural defects, chemical functionalization, opening of individual tubes, and unbundling of SWCNT ropes. Hence, it is hard to understand how the purification treatments can lead to distinct CNT electrochemical performance. Authors have associated these differences with specific structural and chemical features of the CNT samples, but the role that CNT purity plays in such diverse behavior remains poorly investigated. For example, the intrinsic experimental specific capacity of SWCNT bundles is not clear yet.

In this context, lithium electrointercalation in CNT network electrodes still merits investigation, especially when it comes to the effect that potential impurities exert on electrode performance. Together with CNT sample heterogeneity, the electrode preparation protocols can strongly influence the electrochemical behavior of CNT materials in lithium batteries and supercapacitors, because they will determine the network architecture that CNTs will adopt on the electrode. In fact, quantitative nanoscale visualization has demonstrated that a random SWCNT network with architecture that depends on electrode preparation protocols, presents heterogeneous electron transfer kinetics as demonstrated by quantitative nanoscale visualization. In other words, SWCNTs located in different regions of the electrode can display different intrinsic electrochemical activity [11]. Therefore, measuring transport parameters in this kind of electrodes would be welcome. Here, the galvanostatic intermittent titration technique (GITT) helped us to assess the lithium diffusion mechanisms along an SWCNT network electrode when formation of the passivation layer on the bundles surface was complete.

2. Experimental

The SWCNT raw sample was prepared by the arc-discharge method employing Fe/Ni/Co metal powders (1:1:1 molar ratio, 100 mesh, 99.99%, Alfa Products) as catalyst mixture. The obtained sample was submitted to a multistep purification treatment to remove toluene-soluble impurities, amorphous carbon, metallic impurities, and graphite nanoparticles. A detailed description of the purification treatment and sample characterization has been published elsewhere [12] and is summarized in Table 1, which includes selected characterization results. In brief, the raw (as-prepared) SWCNT sample was submitted to a multi-step purification treatment with a previous Soxhlet extraction with toluene, followed by a liquid-phase oxidation with hot hydrogen peroxide solution, an acidic treatment with a mixture of nitric and hydrofluoric acids in ultrasonic bath, finally a physical separation from a sample dispersion in sodium dodecyl sulfate solution and elimination of surfactant of samples. The thermogravimetric analysis furnished direct evidence of the SWCNT samples degree of purity. In addition, the specific surface area determined from nitrogen adsorption analysis provided insight into the irreversible capacity during the first lithium insertion/extraction cycle.

Before the electrochemical characterization, the samples were dried under vacuum at 100 °C, for 24 h. Network composite electrodes were prepared by spreading a slurred mixture of the active material (95 wt %), polyvinylidene fluoride binder (PVDF, Solvay, 5 wt %), and acetone on copper foil (thickness = 60 μm) by means of a Doctor-blade system. After solvent evaporation, the foils were hot-pressed (2 ton), and the disk-cut electrodes (diameter = 7 mm) were purged under vacuum at 110 °C, for 24 h. The electrochemical characterization was carried out in Swagelok-type cells, which were assembled inside a dry-box (H_2O < 5 ppm) using a Celgard® 2400 separator and ethylene carbonate (EC)/dimethyl carbonate (DMC) with 1.0 mol L^{-1} $LiPF_6$ electrolyte (Selectipur grade). The reference and auxiliary electrodes consisted of metallic lithium. All electrochemical cells employed three-electrode-setup. In the galvanostatic experiments, the electrodes loading was about 9.5 mg cm^{-2}. The electrochemical measurements were conducted on a MacPile II cycler, at room temperature.

Raman data were collected on a Renishaw Raman System 3000 equipped with an Olympus microscope (BTH2). The 514.5-nm line of an air-cooled Ar^+ laser was used as the excitation radiation. The galvanostatic intermittent titration technique (GITT) was applied to study the lithium extraction process. For this purpose, the cell was galvanostatically discharged and charged for five consecutive times. At the end of the assay, the cell containing inserted lithium remained in the discharged state. The following conditions were employed during GITT: current pulses of 100 μA for 0.1 h, relaxation for 2 h, potential ranging from 0 to 2.7 V. The TEM analysis was performed on a JEOL–JEM 3010 at 300 KV; the preparation of the samples involved dispersion of materials in isopropyl alcohol that was dropped onto lacey-carbon/copper grids (300 mesh).

3. Results and discussion

Fig. 1 shows the TEM images of the purified SWCNT samples (see sample designations in Table 1). The TEM image of the *Sox_NT* sample (Fig. 1A) revealed a high number of SWCNT bundles, amorphous carbon, and catalyst residues (black dots). TEM analysis of the *Perox_NT* sample (see Fig. 1B) indicated that treatment with hydrogen peroxide completely removed amorphous carbon and concentrated metallic catalyst in the SWCNTs; graphite particles still existed along the sample. A multi-shell graphitic carbon cage covered the catalyst particles, the SWCNT bundles remained well ordered, and hardly any damage occurred to the tubes. Representative images of the *HNF_NT* sample (Fig. 1C) demonstrated that the acid treatment efficiently removed most of the catalyst residue.

Table 1
Description of the analyzed set of SWCNT purified samples employed to prepare the three-dimensional single-walled carbon nanotube bundles network electrode. The description includes the applied purification procedure, the removed impurities, the weight loss temperatures revealed by thermogravimetric analysis, and the specific surface area (SSE) obtained from nitrogen adsorption (BET analysis).

Sample#	Purification procedure	Removed impurities	T (°C)[a]	SSE (m^2 g^{-1})
AP_NT	Raw (as-prepared) sample	–	415 and 703	137
Sox_NT	*AP_NT* submitted to Soxhlet extraction with toluene	Fullerenes and soluble impurities	361 and 680	169
Perox_NT	*Sox_NT* submitted to liquid-phase oxidation with 10% H_2O_2 solution	Amorphous carbon	450 and 725	102
HNF_NT	*Perox_NT* submitted to acid treatment with an HNO_3/HF + SDS[b] mixture	Metal and oxide particles	522 and 740	106
SDS_NT	*HNF_NT* submitted to physical separation from a an SDS[b] dispersion	Graphite nanoparticles	548	116

[a] These temperatures correspond to the derivative curve peaks resulting from the thermogravimetric analysis reported in reference [12].
[b] SDS – Sodium Dodecyl Sulfate.

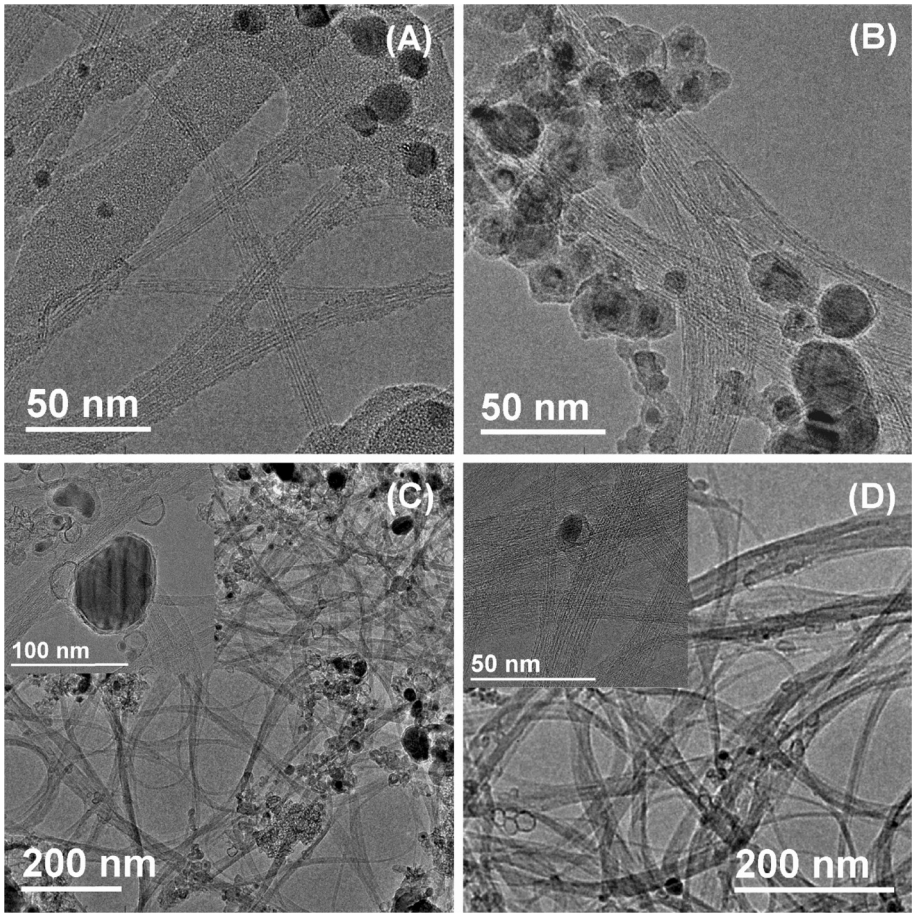

Fig. 1. Typical TEM images of the purified set of SWCNT samples. (A) Soxhlet-purified sample (*Sox_NT*), (B) peroxide-treated sample (*Perox_NT*), (C) acid-treated sample (*HNF_NT*), and (D) high-purity sample from physical separation (*SDS_NT*). The insets depict details of the respective sample.

Although the carbon cage may have protected a few metallic particles from acid attack, these carbon shells experienced partial damage, which removed the metal from the sample and generated a large number of hollow graphitic carbon-shells. Fig. 1D contains a representative image of the *SDS_NT* sample; it attests to the high-purity of the well-structured SWCNT bundles and shows that the purification steps were mild and removed most of the graphitic carbon-shells.

TEM imaging and Raman Spectroscopy (Fig. 2) confirmed the high quality of the *SDS_NT* sample. Indeed, the large I_G/I_D intensity ratio suggested that the sample was highly pure, exhibited few defects, and consisted mainly of nanotubes with a metallic character. The G-band shape confirmed the latter feature: this band is broader and asymmetric for metallic tubes as compared with semiconducting tubes [13]. In addition, the radial breathing modes (RBMs) at low energy helped us to infer the SWCNT diameter (d) through the relation $\omega_{RBM} \approx (224/d^{-1}\ \mathrm{cm}^{-1}\ \mathrm{nm}) + 14\ \mathrm{cm}^{-1}$ [13], where the values 224 and 14 cm^{-1} are empirical constants attributed to environmental effects and inter-tube interactions, respectively. Hence, the highly intense RBM mode at 199 cm^{-1} suggested that the tubes measured 1.2 nm, as confirmed by previous TEM analysis reported in the reference [12].

Cyclic voltammetry of the *Sox_NT* and *SDS_NT* network electrodes with provided insight into the electrochemical lithium insertion/extraction process. Fig. 3 presents the initial cycles of electrodes with different mass loadings. The first lithium insertion curve was significantly different from the subsequent ones. An intense cathodic peak appeared at 0.55 V, because the electrolyte decomposed and a passivation layer or SEI (Solid Electrolyte Interphase) emerged. This decomposition process is typical of carbon-based materials [14], and associated with different areas under the peaks. A comparison between Fig. 3A and B indicated similar lithium insertion/extraction processes; however, it evidenced quite different voltage profiles and associated charges. The *Sox_NT* network electrode (prepared with the SWCNT sample free

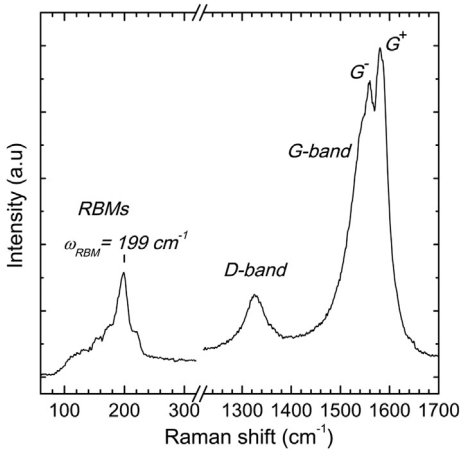

Fig. 2. Raman spectra of the high-purity *SDS_NT* sample indicating the radial breathing modes (*RBMs*), the D-band, and the tangential modes (G-band).

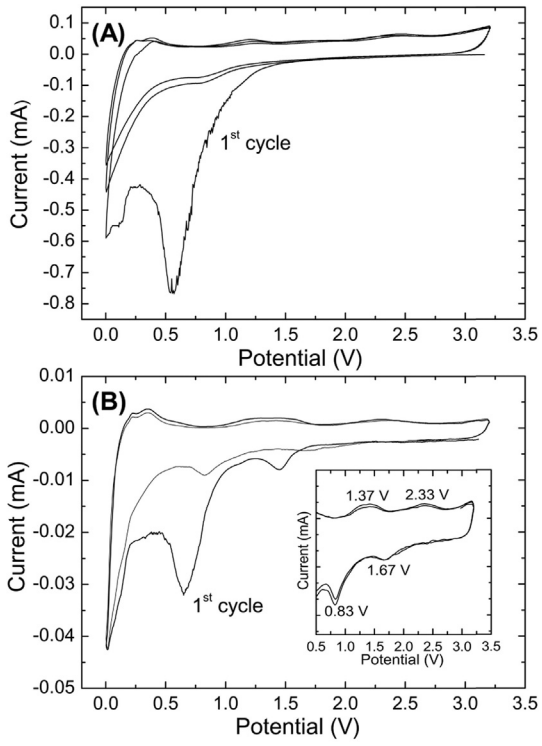

Fig. 3. Cyclic voltammograms obtained for the SWCNT bundles network electrodes (A) *Sox_NT* and (B) *SDS_NT* in $LiPF_6$ 1.0 mol L^{-1} EC/DMC electrolyte at a scan rate of 100 μV s^{-1} from 0 to 3.2 V. The inset shows a magnified view of the 2nd and 3rd cycles.

of fullerenes and soluble impurities) displayed more intense decomposition peak at 0.55 V, because it had large specific surface area (169 m^2 g^{-1}) and contained high concentration of amorphous carbon. Such intense peak is undesirable, because it culminates in irreversible lithium consumption from the lithium ion battery cathodic material. Indeed, the high-purity *SDS_NT* network electrode, which did not contain amorphous carbon, performed better. The inset in Fig. 3B brings a magnified view of the potential region 0.5–3.5 V region. A group of peaks appeared in all of the subsequent cycles, showing that reversible lithium insertion/extraction processes and a capacitive effect occurred simultaneously.

The discharge/charge curves (Fig. 4A–D) obtained for the set of electrodes containing different purified samples agreed with the preliminary cyclic voltammetry results and showed high irreversible capacities during the first discharge/charge cycles. These irreversible capacities (C_{irrev}) are indicated on the cycling behavior plots (Fig. 4E–H). The *Sox_NT* network electrode presented C_{irrev} = 752 mA h g^{-1}, 60% greater than the C_{irrev} of the other investigated samples (≈310 mA h g^{-1}). Therefore, high amorphous carbon concentration (almost 40 wt% before treatment with peroxide) induced excessive electrolyte decomposition. In an operating battery cell, this will happen at the expense of lithium ion originated from the cathode material, resulting in disadvantageous mass balance between the active materials at the electrodes (anode/cathode). The dominant and deleterious role of amorphous carbon also becomes clear when we normalize the irreversible capacities (Fig. 4) by the specific surface area show in Table 1: 4.4, 3.0, 3.0, and 2.7 mAh m^{-2} for the *Sox_NT*, *Perox_NT*, *HNF_NT*, and *SDS_NT* samples, respectively.

In addition, the *Sox_NT* network electrode cycling behavior (Fig. 4E) evidenced progressive capacity fading along the 30 cycles. The mechanical stress associated with lithium insertion into the bundles should be relatively low to reduce adherence between the CNT network and the copper foil substrate, as suggested from the similar ohmic-drop in the several cycles. Amorphous carbon possibly accounted for this high capacity fading. However, the exact role of the amorphous carbon on this effect is still not clear. We know that amorphous carbon coated the tubes in the CNT bundles, as shown in Fig. 1. Because the reversible capacity decreased progressively, while the high coulombic efficiency remained constant,

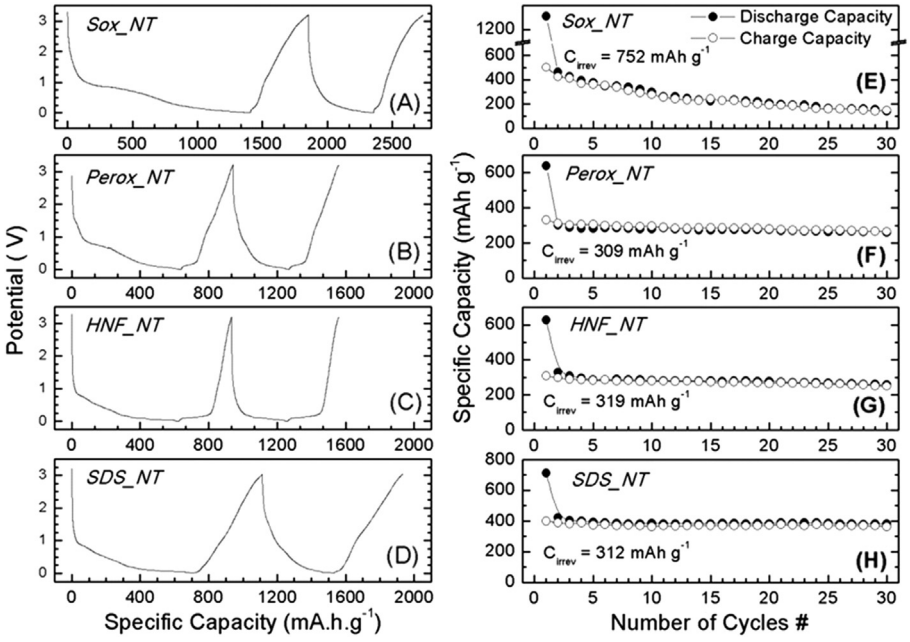

Fig. 4. Initial discharge/charge curves and cycling behavior in terms of discharge and charge capacities obtained for the purified SWCNT bundles network electrodes: (A) and (E) *Sox_NT*, (B) and (F) *Perox_NT*, (C) and (G) *HNF_NT*, (D) and (H) *SDS_NT*, in $LiPF_6$ 1.0 mol L^{-1} EC/DMC electrolyte at a current density of 30 mA g^{-1} from 0 to 3.2 V. The coulombic efficiency of the electrodes as measured for the first four cycles were: 40, 91, 97, and 93% for *Sox_NT*; 52, 97, 95, and 93% for *Perox_NT*; 49, 91, 93, and 97% for *HNF_NT*; and 56, 92, 97, and 97% for *SDS_NT*.

it is possible to suggest a phenomenological model to explain this effect. First, lithium insertion into the nanotube material should induce significant electronic modifications. For example, increased ionic character and diminished π-electrons delocalization might, for instance, promote amorphous carbon redistribution along the nanotube bundles, providing new interaction states. The redistributed carbon could block the access of lithium ions to the sites that had been available in the previous cycles.

The discussion above shows that it is essential to completely remove the amorphous carbon from the samples. The *Perox_NT* network electrode cycling behavior (Fig. 4F) confirmed this—amorphous carbon removal stabilized the specific capacities along the cycles, which was also true for the *HNF_NT* and *SDS_NT* network electrodes (Fig. 4G and H).

Fig. 4A–D illustrate the significant changes in the voltage profiles. The systems stabilized after the 2nd cycle, revealing different behaviors of the voltage response against the state of discharge (SOD). Fig. 5 depicts the 2nd discharge curves of the set of electrodes containing different purified samples. These curves suggested that a combined influence of different impurities determined the voltage profile.

The high-purity network electrode (*SDS_NT*) displayed a lithium insertion curve with a smooth downward slope, indicating that the SWCNT electrode potential modified slowly upon lithium insertion. On the other hand, the discharge curve of the *HNF_NT* network electrode showed a steep voltage drop over the initial lithium insertion and a virtually flat discharge profile at nearly 0.1 V. This behavior resulted from the high concentration of graphite nanoparticles and hollow carbon cages that dominated the voltage profile. Indeed, lithium intercalation occurs in these graphitic nanostructures, to afford a graphite-like discharge curve.

The steep voltage variations observed for graphitic structures resulted from low density of states around the Fermi level, which lithium intercalation promptly modified. Likewise, SWCNTs with a predominant metallic character should hold an effective density of states around the Fermi level [15], which should restrain the electronic contribution to the cell voltage variation. Hence, the smooth sloped curve stemmed mainly from the ionic contribution to the cell voltage; that is, from contribution of the inserted lithium ions activity to the electrode free energy. The electrochemical behavior of the set of electrodes containing different purified samples originated from two predominant contributions – (*i*) lithium intercalation in graphite nanoparticles and hollow carbon cages, and (*ii*) lithium adsorption/insertion into the SWCNT bundles network. The

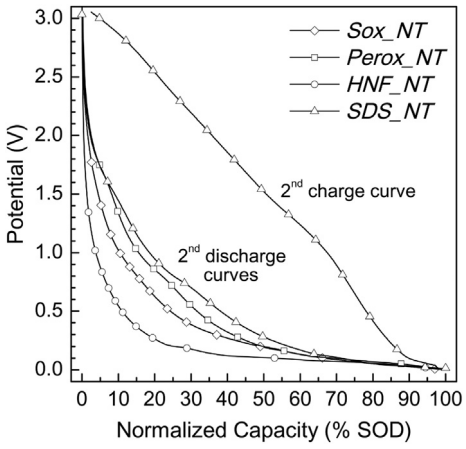

Fig. 5. Second discharge curves (lithium insertion profiles) extracted from the cycling characterization (refers to Fig. 4). The specific capacities were normalized to a state of discharge (% SOD).

Sox_NT and *Perox_NT* network electrodes evidenced combinations of both contributions.

Additionally, it is worth comparing the reversible specific capacity of the several samples. In the 5th discharge/charge cycle, the *SDS_NT*, the *Perox_NT*, and the *HNF_NT* provided 400, 280, 290 mAh g^{-1}, respectively. Therefore, it is clear that impurities such as catalyst, nanographite, carbon cages and amorphous carbon affected the amount of total lithium stored in the electrodes. The lithium storage process predominantly occurred at the carbon nanotubes in different actives sites (which will be discussed ahead). Graphite nanoparticles and carbon cages also contributed to the energy capacity, but in a lower degree. In addition, catalyst and amorphous carbon impurities should be electrochemically inactive for lithium storage. Consequently, the electrode's reversible energy capacity will be higher for the electrodes predominantly constituted by purified carbon nanotubes.

The large voltage hysteresis observed in the consecutive lithium insertion/extraction (discharge/charge) curves (Fig. 4) was noteworthy, too. The second discharge/charge voltage profile in Fig. 4D showed that the *SDS_NT* sample had significant hysteretic behavior. For brevity, Fig. 5 represents these curves in a translated way. The hysteresis over charge/discharge often originates from cell impedance effects associated with overvoltage and high current densities during charge transport or the electrochemical reaction kinetics. However, in the present study, these effects were significantly minimized and they were also observed at different current densities. Hence, the large voltage hysteresis should be attributed to different aspects. First, lithium ions can interact with the carbon atoms along the SWCNT structure; second, lithium ions can adsorb onto several active sites. In the former case, nanotube curvature can elicit distinctive chemical interactions between Li and C atoms and between C atoms. Such interactions are somewhat different from the interactions taking place between lithium-adsorbed graphite with flat carbon sheets. Authors have extensively discussed this model (e.g., Liu et al.) [16]; the nanotube curvature will result in different Li–C and C–C (1.42 Å) bonds, with distinct lengths and ionic characters. In the second case, authors have analyzed lithium ion adsorption as an activated process that has different energy states associated with insertion and extraction. On the basis of these assumptions, lithium extraction should require a higher driving force than lithium insertion. This effect would result in voltage hysteresis, with the charge process occurring at higher voltages. Conversely, the equivalent and uniform Li–C and C–C interactions on the graphite-intercalated compound would induce a somewhat non-hysteretic behavior.

The several active sites types for ion adsorption along the SWCNT bundles should also contribute to the different voltage profiles and hysteresis. It is possible to identify three distinct lithium storage sites: (*i*) lithium attachment on the nanotubes surface, outside the tubes, (*ii*) bare lithium diffusion and adsorption inside the open-ended tubes, and (*iii*) lithium insertion into the bundles arrangements. These storage mechanisms are usually designated as intercalation (*iii*) or alloying (*i* and *ii*) [17]. Several authors have used both theoretical and experimental techniques to study the alloying mechanisms. For example, Zhao et al. [17] applied a first-principle method to study lithium adsorption outside and inside SWCNTs. On the basis of ab initio chemical calculations, Senani et al. [18] suggested that lithium preferably adsorbed inside the tube. Using raw end-closed SWCNTs, Yang et al. [19] proposed a mechanism for surface lithium storage; Shimoda et al. [7] reported experimental results of reversible lithium storage into open-ended SWCNTs.

The SWCNT bundles, held together by van der Waals forces, should intercalate lithium. Song et al. [20] used molecular dynamics simulations to show that the lithium ions penetrated into

the interstitial spaces between neighboring nanotubes. These ions can reversibly inserted between two neighboring tubes. However, lithium adsorption is irreversible when the ions insert between three neighboring tubes, because the very strong adsorption potential made lithium removal from the SWCNT bundles difficult. These effects might underlie the irreversible lithium storage capacity reported in etched SWCNT bundles [21].

To study the diffusion mechanisms of lithium ions into the high-purity *SDS_NT* network electrode, we employed galvanostatic intermittent titration technique (GITT). GITT is a powerful electrochemical method to study the dynamics of lithium battery electrodes. It serves not only to measure chemical diffusion coefficients ($\check{D}_{Li+}$), but also to infer electronic and structural features as well as lithium adsorption mechanisms [22–24]. This technique allowed us to measure the lithium chemical diffusion coefficients ($\check{D}_{Li+}$), the lithium self-diffusion coefficients (D_{Li+}), and the thermodynamic factors (Φ) as a function of the electrode thermodynamic potential. The chemical diffusion coefficient $\check{D}_{Li+}$ is a transport parameter that reflects both the ionic and the electron transport occurring over the active material. It is the coefficient from Fick's first law and relates the transport rate (or flux) in the solid state to the concentration gradient of the diffusing species. $\check{D}_{Li+}$ determines the kinetics of lithium insertion and can be expressed as the product of the self-diffusion (or jump-diffusion) coefficient D_{Li+} and the thermodynamic factor Φ ($\check{D}_{Li+} = D_{Li+} \cdot \Phi$) [25,26]. D_{Li+} and Φ are very sensitive to the structural and electrical properties of ion insertion electrodes, respectively. The D_{Li+} coefficient is a measure of the diffusion that takes place even in the absence of a chemical potential gradient and corresponds to the ionic mobility or viscosity in a solution (Stokes–Einstein equation). The Φ factor measures the chemical potential deviation from that of an ideal solution; it depends on both kinetic parameters (transport number, mobility) and thermodynamic properties (stoichiometry, activity); sometimes it indicates that ionic flux density intensifies due to the simultaneous transport of electrons through the active material. The thermodynamic factor may be larger than 1, which indicates enhanced ion motion attributed the simultaneous electron transport. A Φ value smaller than 1 means that electron immobility slows the ionic species down.

We used the GITT technique to study the high-purity *SDS_NT* sample in a discharged state in short pulse time approximation. To this end, we galvanostatically discharged and charged the electrochemical cell for five consecutive times; in the end, the cell was kept with inserted lithium. Then, we applied galvanostatic titration to extract the lithium ions from the electrode between 0.0 and 2.7 V. We calculated the diffusion parameters ($\check{D}_{Li+}$ and D_{Li+}) as well as the thermodynamic factor (Φ) using Weppner methodologies [24] and also as presented elsewhere [25,26]. Fig. 6 summarizes these results and includes a differential capacity curve (dQ/dV) obtained from the first derivative of the thermodynamic potential curve. We constructed the latter curve on the basis of the GITT analysis; we considered the stationary potential values after the relaxation time and converted the time axis to charge ($Q = i.t$).

The differential capacity curve contained three peaks at 0.13, 1.03, and 2.33 V. These peaks agreed with the cyclic voltammetry results (Fig. 3B) and corresponded to distinct lithium extraction processes from the SWCNT electrode. These extraction processes resulted from the different sites available for lithium storage, as previously classified: (*i*) lithium attachment at the outside surface of the nanotubes, (*ii*) lithium diffusion and adsorption inside the open-ended tubes, and (*iii*) lithium insertion into the bundles arrangements. By analogy with the potential curve of lithium intercalation in graphite, one may infer that the lower voltage peak (0.13 V) stemmed from lithium insertion process into the SWCNT bundles. These bundles interacted via van der Waals forces and behave like a layered graphite structure adsorbing ions at the interstitial spaces.

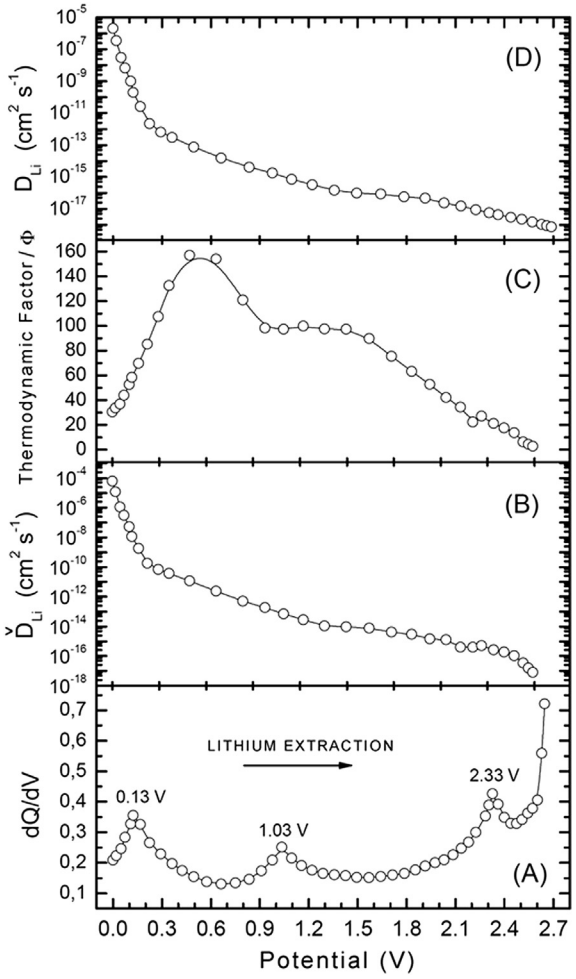

Fig. 6. Transport parameters calculated from the galvanostatic intermittent titration technique for the *SDS_NT* network electrode. (A) Differential capacity curve, (B) chemical diffusion coefficients $\check{D}_{Li+}$, (C) Thermodynamic factor Φ, and (D) self-diffusion coefficients D_{Li+}, as a function of the thermodynamic potential.

While we assigned the peak at 0.13 V to an intercalation process, we attributed the other peaks to the alloying mechanisms (*i*) and (*ii*). Considering that lithium extraction from inside the open-ended tubes would require a larger driving force, (due to thermodynamic and kinetic reasons) one would expect such extraction to occur at higher potentials. Consequently, we assumed that the peak at 2.33 V was due to lithium extraction from the inside of the open-ended nanotubes and ascribed the peak at 1.03 V to lithium adsorption at the external surface. Although the assignments of the peaks at 2.33 and 1.03 V did not rely on experimental evidence, several theoretical works can support these arguments [7,18–20]. The adsorption of lithium atoms inside isolated zigzag CNTs has been shown to be more favorable than lithium adsorption outside these CNTs, because inside the tube the charge transfer from lithium to the CNT is larger [18].

The chemical diffusion coefficient (Fig. 6B) varied from 10^{-4} to 10^{-17} cm^2 s^{-1}, with predominant values around 10^{-12}–10^{-16} cm^2 s^{-1}. Albeit low, these values were higher than those typically observed for lithium electrochemical insertion in other carbon-based materials, such as coke, MCMB (mesocarbon-microbeads), and carbon fibers, with typical values around 10^{-15}–10^{-28} cm^2 s^{-1} [28,29]. In addition, the profile in Fig. 6B indicated an

almost monotonic behavior with significant decrease from 10^{-4} to 10^{-10} cm^2 s^{-1} during the initial Li extraction from 0 to 0.3 V. The extraction at 0.13 V (Fig. 6A) corresponded to lithium inserted into the SWCNT bundles. The high $\check{D}_{Li+}$ values associated with this process (10^{-4}–10^{-9} cm^2 s^{-1}) agreed with lithium diffusion in highly oriented pyrolytic graphite (HOPG), a somewhat similar situation. By combining experimental measurements and theoretical calculations, Persson et al. [30] quantified the lithium diffusion mechanisms in HOPG. These authors demonstrated high diffusivity in the direction parallel to the graphene planes ($\sim 10^{-7}$–10^{-6} cm^2 s^{-1}) as compared with sluggish lithium ion transport along the grain boundaries ($\sim 10^{-11}$ cm^2 s^{-1}). The average $\check{D}_{Li+}$ value from Fig. 6B also corroborated a previous result that Claye and Fischer [31] obtained from electrochemical impedance spectroscopy ($\sim 10^{-12}$ cm^2 s^{-1}).

Additionally, for a more comprehensive analysis, one should remember that the chemical diffusion coefficient corresponds to the product $\check{D}_{Li+} = D_{Li+} \cdot \Phi$; hence, it directly depends on these parameters. A thermodynamic factor greater than 1 should enhance the chemical diffusion coefficients. This convenient situation happened here: values varied from 1 to nearly 160. Fig. 6C revealed an Φ factor with a non-monotonous profile, indicating meaningful electronic variations. This behavior resulted from the explicit Φ dependence on the concentration of the mobile ions (c_i), concentration of the electronic species (c_e), transference number for electrons (t_e), and the charge number (z_i). To obtain a large Φ factor, the concentration of the mobile ions should be higher than the concentration of the electronic species. However, c_i should not be very much larger than c_e, to keep t_e close to 1. Weppner showed that large thermodynamic factors should arise at sufficiently low electron concentration and high electron mobility, requirements that semiconductors commonly fulfill. A metallic character counts on large electron concentration and mobility, typically providing a Φ value close to 1.

Previous works have demonstrated that inserting electron donor species, such as Li, Na, K and Rb, into SWCNT samples should significantly increase the electron transport process [32–35], a consensus among several authors. This phenomenon is an intrinsic property of the SWCNT bundles and originates from partial transfer of valence electrons from the alkali atoms to the carbon antibonding π band. Experimental findings from Larciprete et al. [35] showed that lithium insertion into SWCNT increased the density of states near the Fermi level, suggesting transition from one- to three-dimensional transport behavior in the Li-doped sample. Bendiab et al. [36] also demonstrated that SWCNT samples with Rb doping in a saturated situation underwent transition to a global metallic behavior. Lithium doping should also promote electronic transition in SWNCT due to charge transfer and/or eventual deformation of the tubes [37]. Hence, this metallic character may have strongly influenced the thermodynamic factor (close to 1) at the initial discharged state (with inserted lithium). In this situation, the electron transport did not affect the chemical diffusion, which was equivalent to the self-diffusion coefficient. In parallel with lithium extraction from the interstitial spaces of bundles arrangements, the thermodynamic factor rose continuously to nearly 160. At this state, the chemical diffusion coefficient increased two orders of magnitude as compared with the self-diffusion coefficient. Identifying a reliable reason for this thermodynamic factor behavior is not easy. As stated before, large thermodynamic factors should arise at sufficiently low electron concentration and high electron mobility. A semiconducting character might fulfill both requirements but, in this particular case, specific lithium doping concentrations could induce charge transfer effects, modifying the density of states near the Fermi level and also resulting in a favorable situation. Upon complete lithium extraction at 2.7 V, the SWCNTs should return to their original state, which holds a partial metallic character, as inferred from Raman spectra.

4. Conclusion

In the present study, we determined the transport parameters for SWCNT bundles free of impurities. For the first time, we have demonstrated that GITT provides insight into how transport parameters behave in high-purity and well-characterized SWCNT bundles mounted on a composite electrode using a typical protocol to prepare electrodes for lithium ion battery.

We have also discussed the role that potential impurities play in the SWCNT bundles network electrodes prepared here. This helped understand the divergences arising from several studies about Li intercalation in SWCNT. Amorphous carbon is the impurity to be removed if one wishes to improve electrochemical performance, because it negatively affects the fading capacity and the Faradaic or Coulombic efficiency of the first cycle. We believe that electrochemical parameters reported in the present work are effectively intrinsic parameters of SWCNT bundles with very low concentration of defects, because they are somewhat free of impurities that can influence these values. For example, in the case of closed-packed SWCNT bundles, the number and type of active sites that can adsorb Li during the electrochemical characterization depend on physicochemical modifications. The van der Waals forces that maintain closed-packed SWCNT bundles, the high density of surface active sites (defects, functional groups, nanomaterials), and the presence of open-end tubes can improve the energy density and specific capacity at the expense of the voltage response of charge/discharge curves, eliciting a non-monotonic behavior associated with CNT bundles.

Acknowledgments

The authors thank FAPESP (2010/07681-5) and the National Institute of Science and Technology Carbon Nanomaterials for financial support. They also thank the Electron Microscopy Laboratory–Brazilian Nanotechnology National Laboratory for the electron microscopy facilities and technical support.

References

[1] C. de las Casas, W. Li, J. Power Sources 208 (2012) 74–78.
[2] B.J. Landi, M.J. Ganter, C.D. Cress, R.A. Di Leo, R.P. Raffaelle, Energy Environ. Sci. 2 (2009) 638–654.
[3] J.M. Rosolen, E.Y. Matsubara, M.S. Marchesin, S.M. Lala, L.A. Montoro, S. Tronto, J. Power Sources 162 (2006) 620–628.
[4] B. Gao, A. Kleinhammes, X.P. Tang, C. Bower, L. Fleming, Y. Wu, O. Zhou, Chem. Phys. Lett. 307 (1999) 153–157.
[5] R.S. Morris, B.G. Dixon, T. Gennett, R. Raffaelle, M.J. Heben, J. Power Sources 138 (2004) 277–280.
[6] J.E. Fisher, Acc. Chem. Res. 35 (2002) 1079–1086.
[7] H. Shimoda, B. Gao, X.P. Tang, A. Kleinhammes, L. Fleming, Y. Wu, O. Zhou, Phys. Rev. Lett. 88 (2002), 015502-1–015502-4.
[8] L. Zou, R. Lv, F. Kang, L. Gan, W. Shen, J. Power Sources 184 (2008) 566–569.
[9] V.R. Gonçales, E.Y. Matsubara, J.M. Rosolen, S.I.C. de Torresi, Carbon 49 (2011) 3039–3047.
[10] A.S. Claye, J.E. Fischer, C.B. Huffman, A.G. Rinzler, R.E. Smalley, J. Electrochem. Soc. 147 (2000) 2845–2852.
[11] A.G. Güella, N. Ebejera, M.E. Snowdena, K. McKelveya, J.V. Macphersona, P.R. Unwina, PNAS 109 (2012) 11487–11492.
[12] L.A. Montoro, J.M. Rosolen, Carbon 44 (2006) 3293–3301.
[13] R. Saito, M. Hofmann, G. Dresselhaus, A. Jorio, M.S. Dresselhaus, Adv. Phys. 60 (2011) 413–550.
[14] M. Noel, V. Suryanarayanan, J. Power Sources 111 (2002) 193–209.
[15] S. Guerini, V. Lemos, J. Mendes Filho, L.A. Montoro, E.Y. Matsubara, J.M. Rosolen, Vib. Spectrosc. 45 (2007) 103–107.
[16] Y. Liu, H. Yukawa, M. Morinaga, Comput. Mater. Sci. 30 (2004) 50–54.
[17] J.J. Zhao, A. Buldum, J. Han, J.P. Lu, Phys. Rev. Lett. 85 (2000) 1706–1709.
[18] M. Senami, Y. Lkeda, A. Fukushima, A. Tachibana, AIP Adv. 1 (2011) 042106:1–042116:2.
[19] Z.H. Yang, H.Q. Wu, Mater. Chem. Phys. 71 (2001) 7–11.

[20] B. Song, J. Yang, J. Zhao, H. Fang, Energy Environ. Sci. 4 (2011) 1379–1384.
[21] G.T. Wu, C.S. Wang, X.B. Zhang, H.S. Yang, Z.F. Qi, P.M. He, W.Z. Li, J. Electrochem. Soc. 146 (1999) 1696–1701.
[22] W. Weppner, R.A. Huggins, J. Electrochem Soc. 124 (1977) 1569–1578.
[23] L.A. Montoro, J.M. Rosolen, Electrochim. Acta 49 (2004) 3243–3249.
[24] W. Weppner, in: P. Bruce (Ed.), Solid State Electrochemistry, Cambridge University Press, 1997, pp. 119–228.
[25] C. Wagner, J. Chem. Phys. 21 (1953) 1819–1827.
[26] M. Kizilyalli, J. Corish, R. Metsellar, Pure Appl. Chem. 71 (1999) 1307–1325.
[28] T. Uchida, Y. Morikawa, H. Ikuta, M. Wakihara, K. Suzuki, J. Eletrochem. Soc. 143 (1996) 2606–2610.
[29] P. Liu, H.Q. Wu, Solid State Ionics 92 (1996) 91–97.
[30] K. Persson, V.A. Sethuraman, L.J. Hardwick, Y. Hinuma, Y.S. Meng, A. van der Ven, G. Ceder, J. Phys. Chem. Lett. 1 (2010) 1176–1180.
[31] A. Claye, J.E. Fischer, A. Métrot, Chem. Phys. Lett. 300 (2000) 61–67.
[32] A.S. Claye, N.M. Nemes, A. Janossy, J.E. Fischer, Phys. Rev. B 62 (2000) 4845–4848.
[33] R.S. Lee, H.J. Kim, J.E. Fischer, A. Thess, R.E. Smalley, Nature 388 (1997) 255–257.
[34] R.S. Lee, H.J. Kim, J.E. Fischer, J. Lefebvre, M. Radosavljevic, J. Hone, A.T. Johnson, Phys. Rev. B 61 (2000) 4526–4529.
[35] R. Larciprete, L. Petaccia, S. Lizzit, A. Goldoni, Phys. Rev. B 71 (2005) 115435–115440.
[36] N. Bendiab, L. Spina, A. Zahab, P. Poncharal, C. Marlière, J.L. Bantignies, E. Anglaret, J.L. Sauvajol, Phys. Rev. B 63 (2001) 153407–153411.
[37] X. Yang, J. Ni, Phys. Rev. B 71 (2005) 1654381–1654385.